

Multi-spacecraft observation of plasma dipolarization/injection in the inner magnetosphere

S. V. Apatenkov¹, V. A. Sergeev¹, M. V. Kubyshkina¹, R. Nakamura², W. Baumjohann², A. Runov², I. Alexeev³, A. Fazakerley³, H. Frey⁴, S. Muhlbacher⁵, P. W. Daly⁵, J.-A. Sauvaud⁶, N. Ganushkina⁷, T. Pulkkinen⁷, G. D. Reeves⁸, and Y. Khotyaintsev⁹

¹Institute of Physics, St. Petersburg State University, St. Petersburg, Russia

²Space Research Institute, Austrian Academy of Sciences, Graz, Austria

³Mullard Space Science Laboratory, University College London, UK

⁴Space Science Laboratory, Berkeley, USA

⁵Max Planck Institute for Solar System Research, Katlenburg-Lindau, Germany

⁶Centre d'Etude Spatiale des Rayonnements, Toulouse, France

⁷Finnish Meteorological Institute, Helsinki, Finland

⁸Los Alamos National Laboratory, USA

⁹Swedish Institute of Space Physics, Uppsala, Sweden

Received: 22 September 2006 – Revised: 23 January 2007 – Accepted: 27 February 2007 – Published: 29 March 2007

Abstract. Addressing the origin of the energetic particle injections into the inner magnetosphere, we investigate the 23 February 2004 substorm using a favorable constellation of four Cluster (near perigee), LANL and Geotail spacecraft. Both an energy-dispersed and a dispersionless injection were observed by Cluster crossing the plasma sheet horn, which mapped to 9–12 R_E in the equatorial plane close to the midnight meridian. Two associated narrow equatorward auroral tongues/streamers propagating from the oval poleward boundary could be discerned in the global images obtained by IMAGE/WIC. As compared to the energy-dispersed event, the dispersionless injection front has important distinctions consequently repeated at 4 spacecraft: a simultaneous increase in electron fluxes at energies $\sim 1\text{--}300$ keV, ~ 25 nT increase in B_Z and a local increase by a factor 1.5–1.7 in plasma pressure. The injected plasma was primarily of solar wind origin. We evaluated the change in the injected flux tube configuration during the dipolarization by fitting flux increases observed by the PEACE and RAPID instruments, assuming adiabatic heating and the Liouville theorem. Mapping the locations of the injection front detected by the four spacecraft to the equatorial plane, we estimated the injection front thickness to be $\sim 1 R_E$ and the earthward propagation speed to be $\sim 200\text{--}400$ km/s (at 9–12 R_E). Based on observed injection properties, we suggest that it is the underpopulated flux tubes (bubbles with

enhanced magnetic field and sharp inner front propagating earthward), which accelerate and transport particles into the strong-field dipolar region.

Keywords. Magnetospheric physics (Energetic particles, trapped; Magnetotail; Plasma convection)

1 Introduction

Energetic particle injections (EPI) have been observed and investigated since the first high altitude spacecraft measurements in the inner magnetosphere (e.g. Arnoldy and Chan, 1969). EPI, sharp increases of energetic (tens-hundreds keV) particle flux, are categorized either as energy-dispersed or dispersionless events. In the latter case particle flux increases occur within 1 min for different energies. Late arrival of particles with lower energy inherent to the dispersed events is explained by the azimuthal magnetic drift from the injection place (eastward for electrons, westward for ions), as the velocity is proportional to both the particle energy and the magnetic field gradient; the time of flight effects are negligible for > 50 keV particles. The dispersionless character is explained by the spacecraft being inside the injection region. Long-term continuous observations at geostationary orbit (at 6.6 R_E distance) showed the correlation of EPI occurrence with magnetic activity and the association with substorms. The dispersionless injections were often found near midnight (Baker et al., 1978). Rare two-spacecraft observations

Correspondence to: S. V. Apatenkov
(apatenkov@geo.phys.spbu.ru)

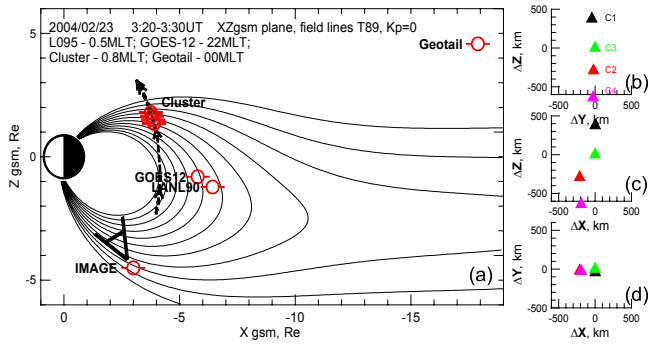


Fig. 1. (a) Spacecraft locations in the XZ_{GSM} projection, (b–d) zoomed-in Cluster XY, XZ, YZ projections show the pearl-on-string configuration.

recorded the earthward propagation of the dispersionless injections with velocities of 10–100 km/s (Moore et al., 1981; Reeves et al., 1996; Sergeev et al., 1998). Earthward velocities of ~ 100 –200 km/s at 8–9 R_E of the magnetic field dipolarization front were documented by Ohtani (1998). The azimuthal extent of the injections is typically about 1–2 local hours, i.e. 2–4 R_E (Reeves et al., 1991; Thomsen et al., 2001).

One of the basic questions concerns the origin of the dispersionless injections observed at geostationary and deeper where the gradient drifts are very strong. A successful model explaining the observed spectra was suggested by Li et al. (1998) and further developed by Sarris et al. (2002) and Zaharia et al. (2004). They traced particle trajectories and estimated energization gained by the particles in the case of the earthward propagating localized structure, an electromagnetic (EM) pulse, which contained an enhanced duskward electric field and its self-consistent magnetic field variation (enhanced B_Z component). Particles, which are transported inside the EM pulse proper during some time, are less affected by the gradient drift that allows them to be injected deeper into the strong magnetic field. This model succeeded in reproducing both observed accelerated fluxes and their dispersionless character (Li et al., 2003). An important requirement for the pulse parameters in these models is a slow (several tens–few hundreds km/s) propagation speed. Such velocities are confirmed by some observations (e.g. ~ 24 km/s on average at around 6.6 R_E by Reeves et al., 1996; ~ 20 km/s at 5–6 R_E by Sergeev et al., 1998), although there are no such slow MHD waves in those regions, where the magnetosonic wave speed is of the order of 1000 km/s. It is only seldom when the opportunity arises to have both comprehensive field and particle observations in the inner magnetosphere (GOES measures only the magnetic field while the LANL instrument suite measures only particles). This makes it difficult to prove the EM pulse model observationally, especially as the injection propagation (direction and velocity)

is difficult to evaluate using single spacecraft data. There is still a great need to obtain a comprehensive description of particle and field signatures of dispersionless injections with the proper distinction between temporal and spatial variations. This is now possible using the four Cluster spacecraft.

In this paper we study both energy dispersed and dispersionless injections observed by the four Cluster spacecraft near perigee during one favorable event. Taking advantage of a well-instrumented multi-spacecraft mission, complemented by data from other spacecraft, we (1) describe the specific properties of dispersionless injections as compared to energy-dispersed ones; (2) show that the dispersionless injection corresponds to a localized spatial structure and estimate its front thickness and propagation speed; (3) perform adiabatic heating calculations to describe the observed electron acceleration and specify the magnetospheric configuration changes associated with a localized injection. Based on the observed injection properties we discuss bursty bulk flows (BBFs) in the magnetotail as the “vehicle” transporting energetic particles into the inner magnetosphere and as a candidate mechanism to produce dispersionless injections.

2 Observations

2.1 Spacecraft configuration and instruments

We start by showing the spacecraft configuration during the period of interest, 23 February 2004, at around 03:27 UT in Fig. 1. Only the projection into the XZ_{GSM} plane is presented, as all spacecraft reside close to the midnight meridian. Magnetic field lines, according to the Tsyganenko (1989) (T89) model with $K_p=0$, are added for reference. The geostationary satellite GOES-12 (hereafter G12) providing ~ 0.5 s resolution magnetometer data was located at about 22:00 MLT. Another geostationary spacecraft, LANL1990-095 (hereafter L095), was at ~ 0.5 MLT and provided energetic particle (electrons and protons $E > 50$ keV) measurements from the SOPA instrument (see Belian et al. (1992) for the instrument description). Geotail was in the northern lobe at $\sim 7 R_E$ above the neutral sheet (at $[-17.8, 0.5, 4.6] R_E$ in GSM coordinates). Southern Hemisphere auroras with a 2-min resolution were observed by the IMAGE spacecraft.

The Cluster quartet had just passed the perigee and was in a pearl-on-string configuration crossing the plasma sheet horns at 0.8 MLT, as illustrated in Fig. 1. The four spacecraft followed each other, moving in the positive Z_{GSM} direction (Figs. 1b, c, d). In terms of the equatorial projection, the Cluster spacecraft moved from the inner magnetosphere outward into the plasma sheet. Independent of the external field model and mapping, C4 was the innermost spacecraft, while C1 was the most tailward spacecraft. The in-situ distance between the leading (C1) and the trailing (C4) spacecraft was ~ 900 km.

A suite of Cluster instruments was used in this study. The magnetic field with a 1-s resolution was available from the FGM fluxgate magnetometer (Balogh et al., 2001). The fluxes of electrons and protons in the energy range 30–300 keV, divided into 8 energy channels, were recorded by the RAPID instrument (Wilken et al., 2001). Lower energy 0.036–24 keV electron fluxes detected by PEACE were available every spin (4 s) with 7.5deg pitch angle resolution (we use 2-D distributions) in 28 energy channels (Johnstone et al., 1997). We also used low energy (<35 keV) ion observations from the CIS instrument (Rème et al., 2001) to estimate plasma pressure and composition change, as well as the electric field from the double probe EFW instrument described in Gustafson et al. (2001).

2.2 23 February 2004 event overview

According to Advanced Composition Explorer (ACE) observations (Figs. 2a, b), the solar wind dynamic pressure and bulk velocity were close to their statistical average values, ~ 2.5 nPa and ~ 420 km/s, respectively; the IMF B_Z component varied around zero not exceeding 6 nT in absolute value. The solar wind parameters are time-shifted to the magnetopause at $X=10 R_E$, using the observed solar wind speed V_X . The B_Z excursion to negative values during 01:00–02:45 UT caused enhanced magnetic flux loading into the magnetosphere and the small substorm commencing at $\sim 02:20$ UT.

A moderate substorm started at $\sim 02:20$ UT as the onset of the negative bay in the magnetic X component registered at the auroral station Narsarsuaq at 23:00 MLT. Situated in the lobe, Geotail observed that the unloading had started at $\sim 02:15$ UT and lasted until 03:30 UT. Geostationary L095 registered a sequence of injections which followed the dropout at $\sim 02:00$ UT, Fig. 2d. G12 located at 21 MLT observed a smooth dipolarization starting at $\sim 02:22$ UT.

The time period of interest 03:15–3:30 UT is characterized by modest geomagnetic activity with AE=200–300 nT. The Dst index was also quiet, reaching its minimum of -11 nT at 03:00 UT. The substorm activation at $\sim 03:15$ UT is seen in Fig. 2 as the AE increase followed by particle injections.

2.3 Energetic particle injections at Cluster and L095

The Cluster quartet observed two separate energetic particle flux increases (EPIs) at $\sim 03:20$ UT and $\sim 03:27$ UT, hereafter “i1” and “i2”, Fig. 3b. Both injections were observed by all four Cluster spacecraft (only Cluster 1 data are shown in Fig. 3b). L095, located deeper and westward as compared to Cluster, observed two separate injections: “i10” at $\sim 03:19$ UT and “i11” at $\sim 03:23$ UT, Fig. 3a.

The injection “i10” was the first injection. “i10” was almost dispersionless, its soft spectrum (almost no flux increase at $E>150$ keV) distinguishes “i10” from the following injections. The next injection, “i1” at Cluster, marked by the

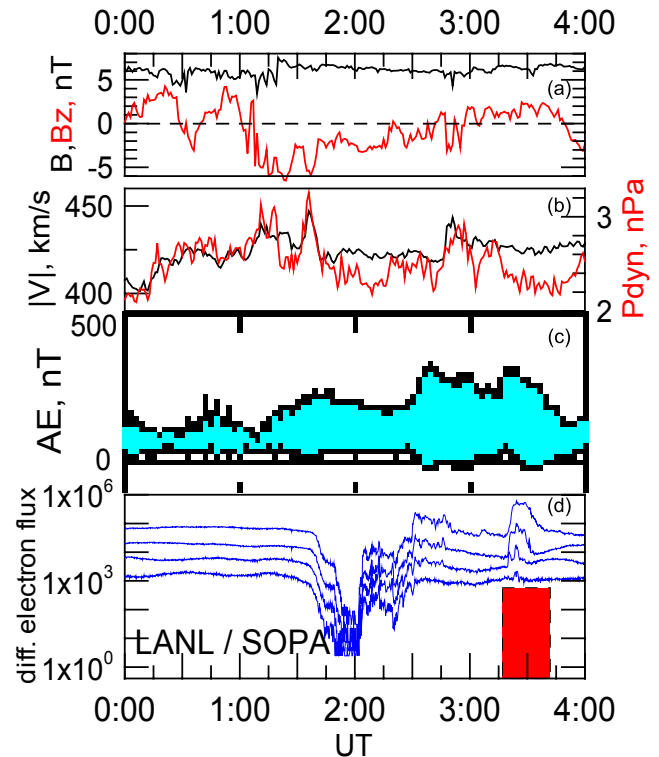


Fig. 2. ACE observations in the solar wind: magnetic field – (a), velocity and pressure – (b) (shifted to $X=10 R_E$). Preliminary AE index (c) and energetic electron fluxes at L095 (d) are also shown. The period of interest is marked by a red bar.

blue dashed line in Fig. 3, was clearly the energy-dispersed injection. Some remnants of the earlier “i10” can be seen in low-energy channels (<68 keV) at Cluster, too. We suppose that the injection “i1” reached the geostationary orbit after a few minutes of inward propagation and was detected at L095 as the injection “i11”.

Using magnetic drift time delays for electrons of different energies we traced particles back in time and obtained an injection start time and MLT location (see, e.g. Reeves et al., 1991). These locations are shown by diamonds in our summary diagram Fig. 5. We should note that the onsets of electron flux increases could not be accurately distinguished for “i1” (low-energy channels) and “i11” due to the pre-existing background level.

At 03:20 UT, within 1 min from “i10” and “i1” detection, a sharp dipolarization front reached G12, located 2 h MLT duskward, and the dipolarization continued to progress afterward until 03:30 UT. However, no sharp magnetic signatures were observed by the Cluster spacecraft related to the energy-dispersed “i1” at around 03:20 UT. The intense and smooth ~ 20 min long bipolar variation in Cluster B_Y (03:20–03:40 UT, Fig. 3c) is rather caused by either the Region 2 field-aligned current sheet or by downward FAC at

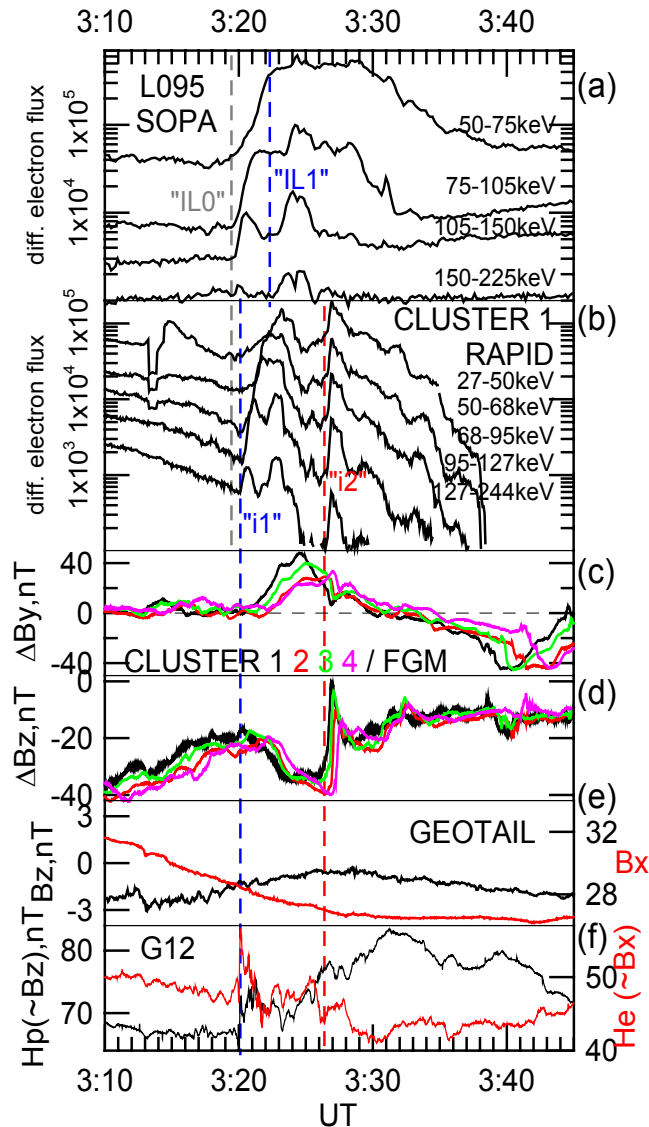


Fig. 3. L095/SOPA energetic electrons (a), Cluster 1/RAPID (b), Cluster FGM B_Y (c); B_Z (d); Geotail B_X and B_Z magnetic field components (e); G12 H_p and H_e (f).

the substorm current wedge eastern edge (Fig. 5); it is hardly related to the particle injections.

The dispersionless injection, “i2”, was observed at $\sim 03:27$ UT by four Cluster spacecraft, but it probably did not reach the geostationary orbit; no injection remnants were found deeper at L095, except for a small flux increase in the 75–105 keV electron channel, Fig. 3a. A similar sharp variation was observed in the magnetic field at Cluster, especially in the B_Z component, which increased by 25–30 nT during ~ 16 s simultaneously with the electron flux growth. A more detailed presentation of Cluster observations will be given in Sect. 3.

2.4 Global auroral observation with IMAGE/WIC

A sequence of auroral images observed by IMAGE/WIC in the Southern Hemisphere is presented in Fig. 4. The background level has been removed, as the auroras were rather faint and the image was visibly affected by direct solar radiation. The bright “oval” visible at $\sim 70^\circ$ CGLat in the dusk-midnight sector is actually only the poleward part of the auroral oval. According to the DMSP F14 flyby at 03:25–03:29 UT in the near-midnight sector, the poleward and equatorward boundaries were located at ~ 71.5 and 63° CGLat, 23:00–24:00 h MLT. Two poleward boundary intensifications, marked “S1” and “S2”, were detected at 03:18 and 03:22 UT. The intensification “S1” showed distinct features of an auroral tongue propagating equatorward. The auroral tongue was most clear and intense at 03:20 UT, but its traces can be seen on the next 3 frames until 03:24 UT at around 22.5 h MLT. The second spot “S2” was weaker and patchy, close to the background level. Its remnants can be discerned until 03:30 UT at a somewhat later MLT (~ 23.5). Also, this auroral feature propagated equatorward. Both intensifications (although rather faint in the equatorward part) resemble auroral streamers in the shape and behavior and may be associated with the electron injections “i1” and “i2”, which were observed 3–4 min after the initiation of poleward intensification at more downward location (Fig. 5).

2.5 Substorm current wedge dynamics

Using mid-latitude ground observations (25 INTERMAGNET stations with magnetic latitudes between 15° and 55°) we calculated the locations and intensity of the substorm current wedge (SCW) (see Sergeev et al., 1996a, for a description of the algorithm). It started to develop at $\sim 02:27$ UT, was centered at about 23:00 MLT, and had a longitudinal width of ~ 3 h in MLT (i.e. L095 was located inside the wedge while G12 was at its western edge, close to the upward FAC).

During the activation of interest at 03:17–03:30 UT, the SCW seemed to develop in the same local time sector and at the background of a still existing and changing SCW from the previous substorm. To minimize the effect of the previous current wedge we processed magnetic variations, taking values at 03:17 UT as a baseline. The corresponding results (although not absolutely accurate due to the problematic baseline choice) are given in Fig. 5, which showed that during the event of interest the second SCW formed between 21:00 and 01:00 MLT, possibly in two steps ($\sim 03:20$ and 03:24 UT, see the intensity variation) corresponding to two injections. The total FAC within this additional SCW reached 0.3 MA at its maximum.

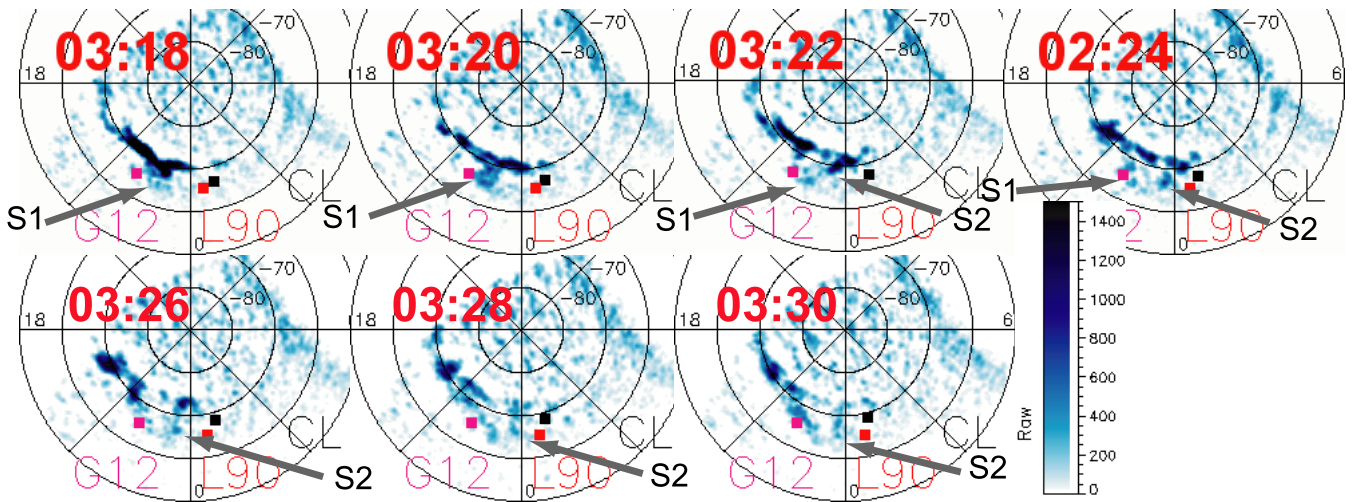


Fig. 4. IMAGE/WIC sequence for the interval 03:16–03:30 UT. Ionospheric footprints of G12, L095 and Cluster spacecraft are shown for reference by rectangles. Faint poleward boundary intensifications (probably streamers) developing equatorward are indicated by arrows “S1” and “S2”.

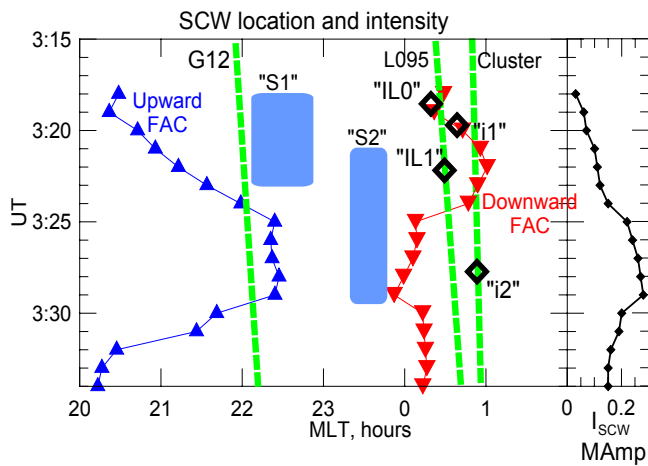


Fig. 5. MLT locations of the SCW upward and downward field-aligned current (left) and SCW intensity in MAmps (right) obtained from analysing midlatitude perturbations. MLT locations of geostationary G12, L095 and Cluster spacecraft (mapped at 7–12 R_E equatorial) are presented by green lines. Locations of auroral poleward boundary intensifications are shown by light-blue bars. The onset times of electron injections observed by L095 and Cluster are shown by black diamonds.

3 Properties of the dispersionless injection as observed by Cluster

The dispersionless injection detected by the well-instrumented Cluster quartet near its perigee gives us a rare opportunity to describe the behavior of different plasma parameters and plasma species observed together with the field variations and to separate spatial and temporal effects.

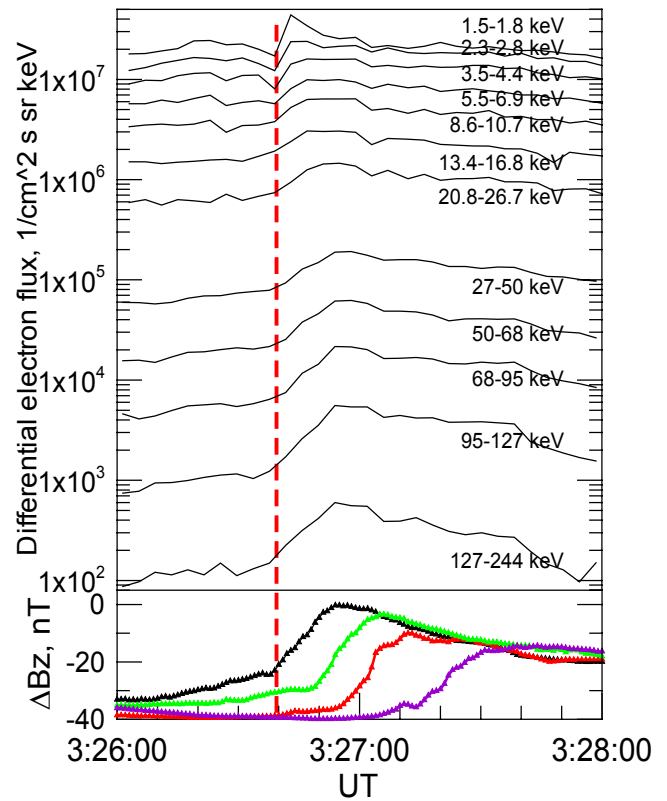


Fig. 6. Differential omni-directional electron flux variations in the energy range 1–150 keV from RAPID and PEACE at C1 (a); B_Z variations at four Cluster spacecraft (b).

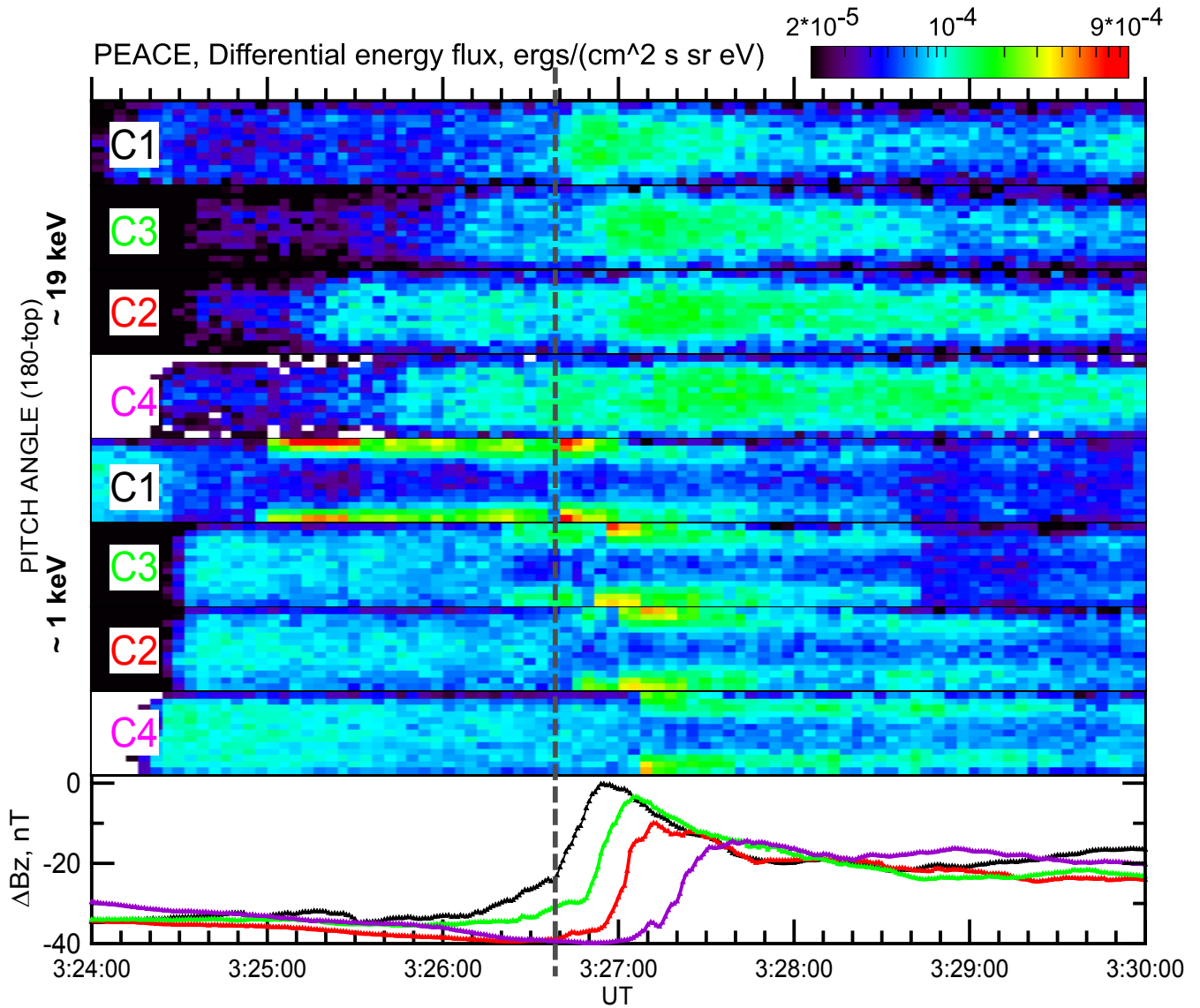


Fig. 7. Pitch-angle plots for high-energy (19 keV) and low-energy (1 keV) components from the Cluster PEACE instrument; 180° (tailward) and 0° (earthward) are at the top and bottom of each plot. Variations in the magnetic field are shown for reference at the bottom panel.

As shown in Sect. 2.3, the dispersionless injections at the four Cluster spacecraft were observed at the same time with the increases in the B_Z magnetic component, Fig. 6. A simultaneous magnetic pulse and electron flux increase were repeated at all four spacecraft; thus, we can definitely associate the injection signatures with a structure propagating past the spacecraft. This propagating structure has a sharp leading front that we call the injection or dipolarization front. The front passes the spacecraft in order from C1 to C4 which reveals a propagation in the negative Z_{GSM} direction, i.e. into the stronger dipole field considering the Cluster satellite locations. The elongated tetrahedron configuration (Figs. 1b–d, Sect. 2.1) allows one only to estimate the local velocity in

the Z -direction, which was found to be ~ 25 km/s (Cluster orbital motion was taken into account). Furthermore, evidence of some deceleration can be noticed. Using this speed and the 15- to 20-s duration of the leading front, we estimate its thickness to be ~ 450 km.

The low energy (< 25 keV) electron observations from the PEACE instrument provided full pitch-angle distributions of this population. Figure 7 shows color-coded electron energy flux versus time where the electron pitch angles correspond to the location in each horizontal bar with 0° at the bottom and 180° at the top of each panel. There were two interesting aspects of the electron pitch-angle behavior: one is a transition from pancake to bi-directional anisotropy at

lower energies (0.1–3 keV). It was observed well before the injection at 03:25:00, 03:26:20 and 03:26:45 UT at spacecraft C1, C3, and C2, respectively (C4 spacecraft recorded a corresponding change at around 03:27:08 UT at the injection front). Based on the spacecraft locations, this boundary seems to be a spatial boundary rather than a temporal one, the in-situ velocity was less than 2 km/s.

Secondly, two kinds of anisotropy were simultaneously observed, a field-aligned anisotropy at $E < 2$ keV and pancake anisotropy at $E > 5$ keV. To demonstrate these two different anisotropies we present in Fig. 7 the pitch angle distributions of the 1 keV and 19 keV electrons. The anisotropy character did not change during the injection front passage; the existing distributions only intensified at the front. One can notice that in all cases the fluxes of earthward low-energy electrons increase, first suggesting that the plasma fills the injected flux tubes in the earthward direction. A sharp change in the anisotropy at lower energies (0.1–3 keV) has been already pointed out above, but it was not associated with the injection.

The low-energy ion behavior during the period of interest was also observed by the CIS instrument. Ion moments with 8-s resolution were available from C1/HIA and C4/CODIF. The hydrogen omnidirectional energy flux spectrogram and the ion pressure from different species are presented in Figs. 8a–d. The spectrogram, Fig. 8a, shows that the 5–20 keV ion population is the main contributor to the energy flux, both before and during the injection. Ionospheric species He+ and O+, Fig. 8b, contribute about ~10% to the pressure while the distinct solar wind-origin ions, He++, provide up to 50% of the pressure. This implies that most of the injected plasma originated from the more distant magnetotail. We also estimated the contribution to the plasma pressure from the energetic ($E > 30$ keV) ions and electrons using the RAPID instrument and found it to be <10% of the ion contribution measured by CIS, Figs. 8c–d. Total pressure values measured immediately before the injection by Cluster 1 gave about 0.4–0.5 nPa, which correspond to equatorial radial distances of 11–12 R_E , according to Tsyganenko and Mukai (2003) under the observed SW conditions (and assuming pressure isotropy). Cluster 4 measures ~0.9 nPa total pressure, which corresponds to 8–9 R_E equatorial distance. We note that the plasma pressure increases by a factor of 1.5–1.7 at both spacecraft during the passage of the injection front (Figs. 8b–d), whether one considers the hydrogen contribution or the total pressure. The ion velocity from C1/HIA is presented in Fig. 8e. The major variation at the front was the change in the V_{ZGSM} component, which reached ~–80 km/s at its extremum. This negative V_Z in situ corresponds to an inward plasma motion, in the same direction as the injection front propagated.

Electric field measurements (GSE X and Y components) from the EFW instrument were also available for this interval, amplitudes up to 40 mV/m were recorded at/near the injection front (see Fig. 9). First, we notice that variations

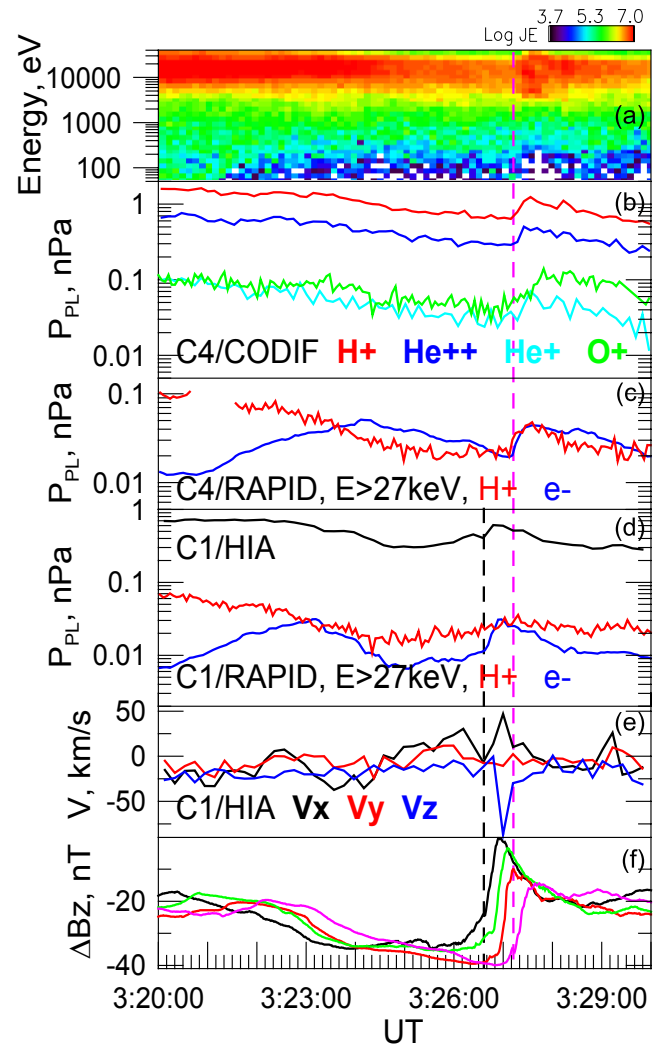


Fig. 8. Cluster 1 and 4 ion and energetic particle observations. Cluster 4: (a) CIS/CODIF H+ omnidirectional energy flux; (b) CIS/CODIF pressure with contribution from different ion species; (c) RAPID (>27 keV) ion and electron pressure. Cluster 1: (d) pressure contributions from CIS/HIA (black) and RAPID; (e) ion velocity from HIA. (f) magnetic pulse in the Z component from all 4 s/c is added for reference.

in E_Y were dominant as compared to E_X . Secondly, the bipolar variation in E_Y repeated at all four s/c, Figs. 9d–g, but the variation amplitude seems to decrease with the pulse propagation past the spacecraft. This is possibly related to the braking of earthward propagation of the injected flux tube. The negative E_Y pulses (corresponding to a dawnward electric field) were observed first together with the onset of sharp B_Z increases. Later, still during the increasing B_Z , E_Y changed to positive values. The duration of the negative pulse was about 3 spacecraft spins (~10 s). The E_Y displayed a turbulent character right after the B_Z maxima, i.e. following the front passage. To obtain an impression of the

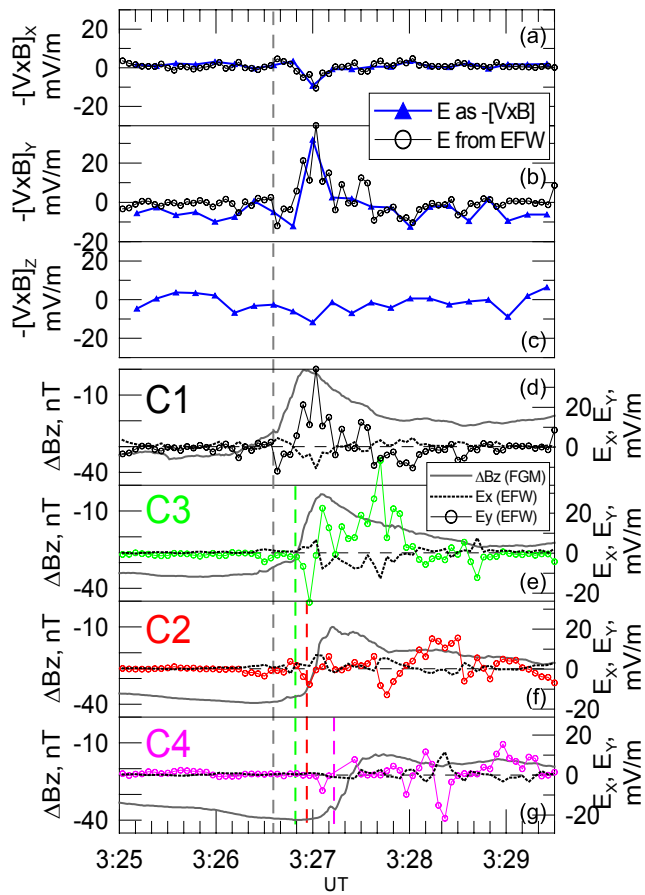


Fig. 9. Flux transfer $-\mathbf{V} \times \mathbf{B}$ estimated from CIS/HIA and FGM observations at C1 compared with the double probe E_X and E_Y (a–c); EFW E_X (dashed) and E_Y electric field, together with FGM B_Z variations at four Cluster spacecraft (d–g).

possible behavior of other E-field components we also plotted in Figs. 9a–c E, computed from $-\mathbf{V} \times \mathbf{B}$ using plasma velocity from Cluster 1/HIA and B-field from FGM. It was found that (1) the X- and Y- components of $-\mathbf{V} \times \mathbf{B}$ are closely associated with E_X and E_Y , respectively, from EFW, and (2) the variation in the $-\mathbf{V} \times \mathbf{B}_Y$ component was the dominant component compared with the components along the tail and in north-south direction.

4 Magnetic configuration and mapping

Although Cluster provided detailed observations of the localized structure associated with the dispersionless plasma injection, these observations were made in the plasma sheet horns, far from the near-equatorial region, where most of the current and magnetic field reconfiguration and plasma acceleration took place. Therefore, we need to specify the magnetic configuration to obtain answers to the following important questions: (a) What is the distance range (also scales and

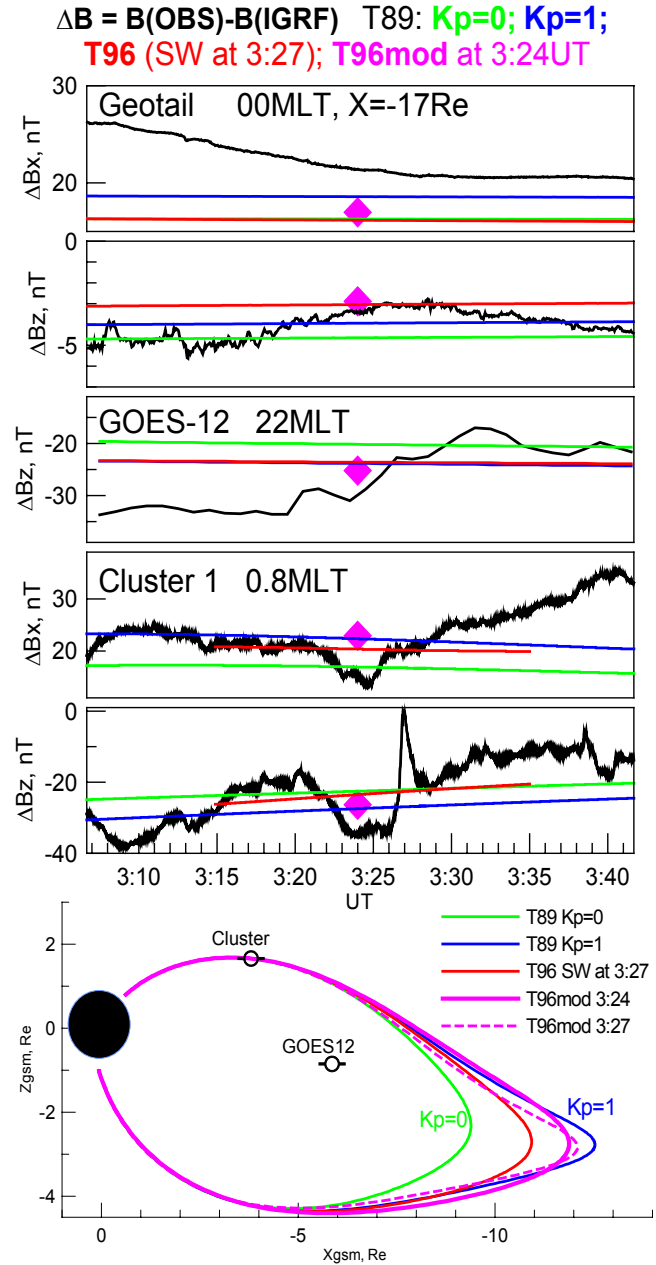


Fig. 10. Magnetic field observations at Geotail, G12, Cluster with dipole field subtracted (a–c) compared with predictions of different models T89, T96, T96mod. Magnetic field lines traced through the Cluster location using different models.

propagation speed) in the equatorial magnetosphere where the localized injection develops? (b) What is the actual geometry change in the earthward contracting plasma tube which contained the accelerated plasma? To specify the magnetic configuration preceding the injection we should first consider the magnetic field perturbations observed by Cluster, by Geotail (in the lobes at $17 R_E$) and by GOES-12 (3 h in MLT duskward from Cluster). The data are shown (with

IGRF field subtracted) in Fig. 10, together with the magnetic fields predicted by the T89 and T96 models. Also the observed magnetic field values were used to tune the parameters of the T96 model (by varying the intensity of the tail current and ring current systems to obtain the best fit to the observations; see Kubyshkina et al. (1999) for the method description). This best fit model (the diamonds T96mod in Fig. 10) for 03:24 UT provides nearly the same magnetic field and similar Cluster field line shape as the $K_p=1$ T89 model does. According to these comparisons, the tail configuration before the injection (at the state 1) is only moderately stretched, and the equatorial crossing distance of the Cluster field line is between 10 and 13 R_E for the best-fit models (Fig. 10). This method cannot, however, be applied to specify the final state of the injected flux tube.

Still, the spacecraft coverage is far from optimum in this case, so we also tried another (relatively independent) method to specify the equatorial location and, most importantly, to constrain the change between the initial state and the final stage (when the injection peak was observed at the Cluster location) of the localized injected plasma flux tube. As in some previous studies (Delcourt et al., 1992; Smets et al., 1999), we assume that the major flux tube geometry change is due to the dipolarization and contraction (earthward motion) of its equatorial part (due to the change/redistribution of the tail currents and resulting inductive electric field), whereas the change in its ionospheric footpoint is insignificant, because the process is very short in duration. This situation, as schematically shown in Fig. 11, means that the initial (1) and final (2) flux tube locations are close to each other in the plasma sheet horns probed by Cluster, so that a comparison of the accelerated electron spectra in the peak of the event (state 2) with those observed just before the event (state 1 in Fig. 11) can be used to characterize the amount of acceleration in the contracting plasma tube.

To realize this idea, we used the following scheme (see details in Appendix). We used the K_p -dependent T89 model by introducing a non-integer K_p^* (the corresponding model field was computed by the linear interpolation between the field values in two neighboring integer K_p models). We compared the amount of electron acceleration in the adiabatic approximation between the two configurations (1 and 2 in Fig. 11, characterized by initial Kp_1^* and final Kp_2^* values, respectively) of the field line passing through the location of Cluster-1 (see details in the Appendix). By doing this we specify the change in the properties of one particular flux tube rather than determine the entire magnetic configuration change. We tried different Kp_1^* values in the range 0.5–1.5 (with 0.1 step), motivated by the previous observation that the $K_p=1$ model fits best to the B-fields observed just prior to the injection. For each Kp_1^* we varied the Kp_2^* value (also with 0.1 step) to find the best match to the electron acceleration expected on the field line which is passed through the C1 location. The results are given in Table 1, the fit goodness measure, σ , in logarithmic scale, is also shown.

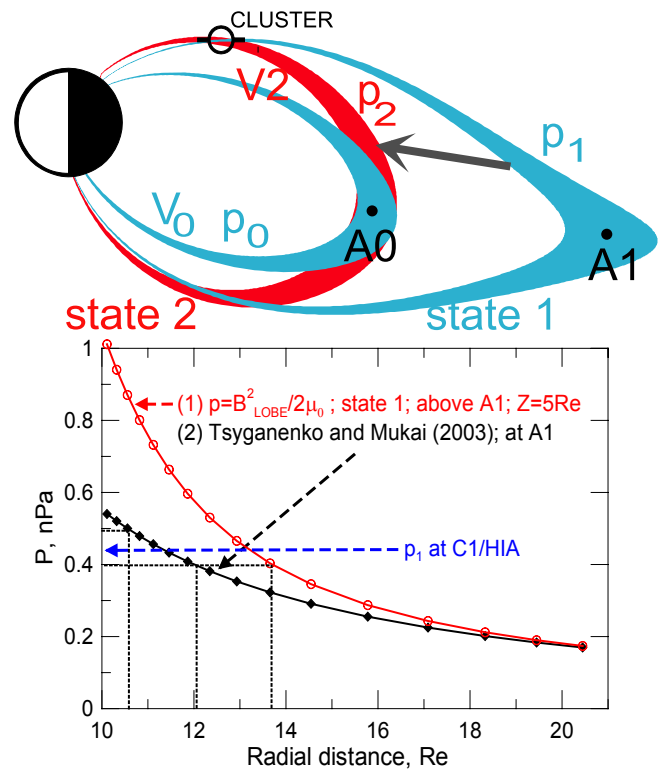


Fig. 11. Sketch explaining the dipolarization and entropy comparisons (top). Cluster 1 pressure value before the injection compared with empirical pressure profile of plasma sheet ions by Tsyganenko and Mukai (2003) and with magnetic pressure in lobes $Z=5 R_E$ above A1 point (bottom).

As seen from Table 1, the acceleration is reproduced with the smallest errors ($\sigma=0.20$ – 0.21) when the initial flux tube location was at 10–12 R_E distance range. We should also note that the σ value is sensitive to the change between the flux tube states 1 and 2 more than to its initial location (state 1). To clarify and limit the initial equatorial location we use the observed plasma pressure as an additional filter. The pressure is computed in the equatorial section of flux tube 1 from the empirical plasma model by Tsyganenko and Mukai (2003), P_{1TM03} . We compared P_{1TM03} with the observations to indicate if an initial state was realistic or not. The comparison in Fig. 11b indicates that the observed pressure (~ 0.4 nPa at C1 and ~ 0.9 nPa C4 before the injection) could only be observed at distances 9–13 R_E . The possible underestimation of the equatorial pressure measured by the CIS instrument (e.g. due to presence of heavy ions) favors the closer initial flux tube location. This eliminates the bottom part of Table 1 as unrealistic and allows one to identify the initial location to be at <11 – $13 R_E$ radial distances.

Previously, observations in this distance range were presented by Ohtani (1998), who obtained an earthward propagation speed of ~ 200 km/s, which corresponds to the lower

Table 1. Different Kp^* pairs, standard deviation, injection front observed at C1 and C4 mapped to the equatorial plane, front propagation speed, front thickness, initial pressure obtained from Tsyganenko and Mukai (2003) and vertical pressure balance. The injected flux tube parameters (pressure, volume, entropy) related to those in the neighbouring flux tubes.

Kp_1^*	Kp_2^*	σ	$R_1 \rightarrow R_2, R_E$	$V_{EQ}, \text{ km/s}$	D_{front}, R_E	$P_{1\text{TM03}}, \text{ nPa}$	$P_{1\text{LOBE}}$	$\frac{P_2}{P_0}$	$\left(\frac{V_2}{V_0}\right)^{5/3}$	$\frac{P_2 V_2^{5/3}}{P_0 V_0^{5/3}}$
0.5	0.0	0.23	10.1→8.7	241	0.61	0.43	0.66	1.05	1.01	1.06
0.6	0.1	0.21	10.3→8.8	258	0.65	0.41	0.60	1.06	1.00	1.06
0.7	0.2	0.21	10.5→8.9	275	0.69	0.38	0.53	1.07	1.00	1.07
0.8	0.4	0.20	11.0→9.2	310	0.78	0.35	0.46	1.15	0.99	1.14
0.9	0.6	0.20	11.6→9.4	379	0.95	0.32	0.40	1.23	0.97	1.19
1.0	0.7	0.21	12.0→9.6	413	1.04	0.29	0.35	1.24	0.95	1.18
1.1	0.9	0.20	13.0→9.9	534	1.34	0.26	0.28	1.32	0.96	1.27
1.2	1.0	0.23	13.7→10.0	637	1.60	0.23	0.24	1.33	0.97	1.29
1.3	1.1	0.25	14.6→10.3	740	1.86	0.20	0.21	1.34	0.97	1.30
1.4	1.2	0.25	15.8→10.6	895	2.25	0.18	0.19	1.36	0.98	1.33
1.5	1.3	0.23	17.0→10.9	1154	2.90	0.17	0.17	1.37	0.99	1.36

limit of our estimate. With the initial location of the injected plasma tube in the range of 11–13 R_E , the propagation speed mapped to the equatorial region is 200–400 km/s, and the spatial scale of the frontside layer is about 1 R_E . The distance range of the flux tube contraction and velocities are comparable to those used in the EM pulse simulations by Li et al. (1998). They used 100 km/s velocity EM pulse, which was initiated at 40 R_E to describe the observations at 6.6 R_E .

Having in mind the picture of an azimuthally localized injected plasma tube we may attempt to compare this flux tube (at final state 2) with the flux tube at the same distance but at a different longitude, outside the injection sector (flux tube 0 in Fig. 11). To do that we assume that the ambient plasma and magnetic configuration are not strongly affected during the localized injection (or that the injected flux tube has a small azimuthal extent). In this case we can use the state 1 model with Kp_1^* to specify the parameters of plasma flux tube 0 and state 2 model with Kp_2^* to specify the parameters of the plasma tube 2. From these models we can easily compute the volumes of the unit magnetic flux tube ($V = \int ds/B$) at these locations. Also, by assuming force equilibrium in the midnight equatorial plane ($\nabla P = [\mathbf{j} \times \mathbf{B}]$), we may compute the plasma pressure at the point A0 from the Kp_1^* model by integrating ∇P along the tail axis from point A1 to the point A0 as $P_0 = P_1 + \int_{A1}^{A0} [j \times B] dl$. Here the pressure P_1 observed by Cluster before the injection is used as the initial value, whereas the cross tail current density (j) and magnetic field (B_Z) in the neutral sheet are computed from the state 1 model (see Kubyskhina et al. (2002) for method testing).

The results of computation (Table 1) show that in the equatorial plane the pressure in the injected tube is comparable to that in the neighboring flux tubes (in MLT sense) ($P_2 \sim P_0$), in spite of the noticeable pressure increase during the injection ($P_2 \approx 1.5\text{--}1.7 P_1$). The net change in the plasma tube entropy

parameter $P V^{5/3}$ is such that the entropy of the injected flux tube is still comparable with the value in the ambient flux tubes, $P_2 V_2^{5/3} / P_0 V_0^{5/3} \sim 1.0$ at the final observation location. This implies that the injected plasma parcel may have had a property of a plasma bubble during the earlier stages of its evolution. This is consistent with the conclusions of the previous case and statistical studies of fast flow bursts in the magnetotail (e.g. Sergeev et al., 1996b; Schödel et al., 2001; Nakamura et al., 2001b; Lyons et al., 2003).

5 Discussion

5.1 Summary of observations

Both energy-dispersed and dispersionless injections were observed at LANL and Cluster satellites near the midnight meridian. The similarity in the activity associated with the energy-dispersed and the dispersionless injections allows us to interpret them as similar objects and prescribe the different appearance to the different spacecraft locations with respect to the injection proper. We summarize our observations:

1) As compared to the dispersed injection “i1” which had no stable signatures in the magnetic and electric field the dispersionless injection “i2” (observed at Cluster) had the following distinctive properties repeated at all 4 spacecraft: (a) a simultaneous increase in the electron fluxes at all energies between 1 and 300 keV during ~ 16 s (“injection front”); (b) an increase in the B_Z magnetic field component by ~ 30 nT at the dipolarization front; (c) an increase in the plasma pressure by a factor of 1.5–1.7 at the dipolarization front; (d) a bipolar-like turbulent variation in the electric field E_Y component, first a negative then a positive pulse with an amplitude of $\sim 10\text{--}40$ mV/m at the dipolarization front. Observed

by all 4 satellites with appropriate time shift, these properties characterize the spatial structure associated with dispersionless injections.

2) Four spacecraft allowed us to identify a sharp injection/dipolarization front that propagated inward, with a propagation speed and front thickness estimated to be ~ 25 km/s (with some deceleration) and 400 km, respectively, at the observation region in the plasma sheet horns, at $5 R_E$ geocentric distance, where the magnetic field magnitude was 600 nT. After tuning the magnetic field model and mapping to the equatorial distance at $R \sim 9\text{--}12 R_E$, we obtain (see Sect. 4) an earthward velocity of $V \sim 200\text{--}400$ km/s and a thickness of $\sim 1 R_E$ in the equatorial plane.

3) Based on IMAGE/WIC observations we attempted to identify auroral structures detected together with injections. The auroral oval was rather faint with poleward/equatorward boundaries at $\sim 71.5/63^\circ$ from the DMSP F14 flyby at 03:25–03:29 UT. Two poleward boundary intensifications (marked by “S1” and “S2” in Fig. 4), propagating equatorward, had lifetimes of 4–6 min, as observed by IMAGE/WIC, and could possibly be associated with the injections observed by LANL and Cluster at perigee. “S1”, initiated at 03:18 UT, was possibly related to injection “i1” at 03:19 UT, and “S2”, initiated at 03:22 UT, was possibly associated with the dispersionless injection “i2” at 03:27 UT.

4) Electron pitch angle distributions observed by PEACE (0.05–27 keV) showed two kinds of anisotropy, bi-directional at $E < 2$ keV and pancake at $E > 5$ keV. A sharp inner boundary of the bi-directional distributions (at 0.1–3 keV) was found before (i.e. deeper inside the magnetosphere) than the injection, mapping at a $8\text{--}10 R_E$ distance in the equatorial plane. This boundary seemed to be spatially stable and was unrelated to the injection, and this will be a subject of a future study. The character of the electron anisotropy did not change while the particle flux increased during the injection front passage.

The properties of the dispersionless injection front confirm that we observed a localized plasma structure passing the chain of Cluster spacecraft. Its localization in the azimuthal direction is supported by narrow auroral structures and by the absence of magnetic pulse signatures at the G12, which was only 2 h in MLT away from the injection observations. We clearly see that the pulse associated with the dispersionless injection was spatially localized in the radial direction: spacecraft C4 did not record any changes at the time when the peak of the structure had already passed over the C1 satellite, 900 km away (see Fig. 9). There were no global changes in the magnetic field, electric field, or plasma properties. When using the term “dipolarization” or “dipolarization front”, we therefore mean azimuthally and radially localized reconfiguration or propagating structure.

5.2 On the origin of plasma injections

Plasma injections, observed fluxes and dispersed/dispersionless character, are simulated using the EM pulse model (Li et al., 1998; Sarris et al., 2002; Zaharia et al., 2004). These simulations describe the observations at the geostationary orbit, $6.6 R_E$, and deeper, requiring an earthward propagating structure with several tens–few hundreds km/s velocity, and enhanced duskward electric and northward magnetic fields. In this paper we presented multipoint observation of the dispersionless injection at a larger radial distance of $8\text{--}13 R_E$, where only a few injection observations have been done previously. The observed injection properties, propagation velocity, and electric and magnetic fields mostly fit the EM pulse requirements. This supports the EM pulse idea, although it is not yet clear what generates such structures and transports them earthward (e.g. there is no MHD wave propagating with such a slow speed).

We suppose bursty bulk flows (BBFs) propagating as a plasma structure (not a wave) to be responsible for the EM pulse transport and, thereby, the energetic particle origin. The observed dispersionless injection structure mapping at $8\text{--}13 R_E$ propagated $\sim 2 R_E$ earthward at a 200–400 km/s speed. The similar velocities are known for rapid flux transfer events (RFT) at this distance (~ 200 km/s, on average, after Schödel et al., 2001). So, BBFs satisfy (1) the velocity limits; (2) azimuthal extent limits, both required for the EM pulse model and observed for the injections; (3) enhanced B_Z and enhanced E_Y (e.g. Sergeev et al., 1996b). BBFs, however, are mostly studied at a $10\text{--}15 R_E$ radial distance and are difficult to observe closer to Earth due to a velocity decrease (Schödel et al., 2001) and, probably, an occurrence decrease. We also discussed the possible connection between the injections and auroral streamers that was recently investigated by Sergeev et al. (2005). Streamers, in turn, are known to be associated with BBFs (Sergeev et al., 1999, 2000; Nakamura et al., 2001a; Lyons et al., 2002).

Our detailed observations of the injection in the transition region ($8\text{--}13 R_E$) provide a link between the EM pulse (considered in the inner region) and BBFs (studied at $> 10 R_E$) previously discussed as separate phenomena. We suggest that fast narrow plasma streams (BBFs), which have the bubble property, are the very probable mechanism of plasma injections into the inner magnetosphere.

Appendix A

Modeling of adiabatic heating

After selecting the magnetic field models which describe the distribution of the magnetic field along field lines 1 and 2 (Fig. 11), passing through the observation point (CL), we compute the electron acceleration during the magnetic field reconfiguration following the approach by Smets et al.

CLUSTER 1 **Initial** 3 spin averaged 3:26:31-39 compared with **final** 3:26:43-51
Field line fixed at SC location; transition from T89 Kp*=0.5 tp Kp*=0.0

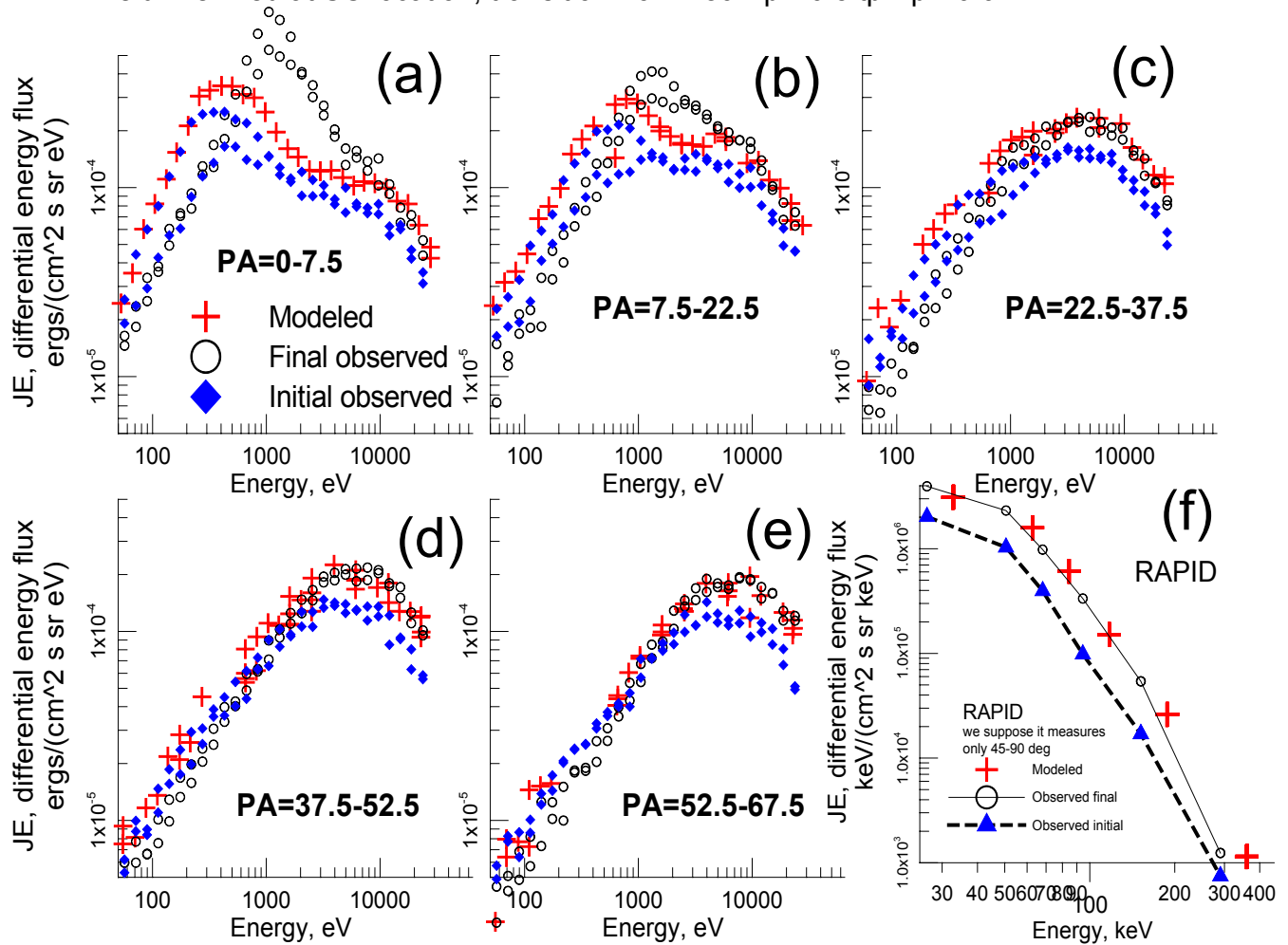


Fig. A1. Comparison of electron spectra observed before (blue diamonds) and after (black circles) the injection with the modeled spectra (red pluses). Panels (a–e) correspond to different pitch angles at PEACE, higher energy spectra part from RAPID is at panel (f).

(1999). We assume conservation of the first two adiabatic invariants for electrons, as well as phase space density (Liouville theorem).

As input data we use Cluster/PEACE observations from 30 energy channels in the range 0.036–24 keV for electrons with a 15-degree pitch angle resolution. Taking every energy and every pitch angle bin and using observed initial (before the injection) differential energy flux $J_E(W_1, \alpha_{CL})$ we do the following:

- (1) Transform the pitch angle from the Cluster location to the equatorial plane using the magnetic configuration in state 1 to obtain $J_E(W_1, \alpha_{EQ})$ (in-situ pitch angles are mapped to the equatorial ones using $\sin^2 \alpha_{EQ} = \sin^2 \alpha_{CL} \cdot B_{EQ}/B_{CL}$);
- (2) Calculate the increase in the perpendicular energy component due to betatron acceleration (from conservation of the magnetic moment) as $W_{\text{perp}2} = W_{\text{perp}1} \cdot B_{eq2}/B_{eq1}$;

- (3) Calculate the increase of the parallel energy component using the second adiabatic invariant conservation, $W_{\text{par}2} = W_{\text{par}1} \cdot FL_1^2/FL_2^2$, where FL1 and FL2 are the field line lengths between the mirror points in states 1 and 2. Since the mirror point locations (FL1, FL2 as well) depend on the particle pitch angles, an iterative search is required. Prescribing minimum and maximum W_{par} values (which correspond to minimum and maximum of the longitudinal invariant $J_2 = W_{\text{par}2} \cdot FL_2^2$ as well), we use the dichotomy algorithm to satisfy J_2 approaching J_1 to an accuracy less than 0.1%;

- (4) Using the Liouville theorem ($f(W, a) = J_E/W^2 = \text{const}$) we obtain the new energy flux value $J_E(W_2, a_2)$;

- (5) Transform the pitch angle distribution from the equatorial plane to the Cluster location (as in (1)).

In the case of Cluster observations we distribute the modeled fluxes among the bins for energies and pitch angles used by the Cluster/PEACE instrument. Choosing the initial Kp_1^* , and taking the spectrum before the injection, $J_E^1(W, \alpha)$, we compute the model flux $J_E^{\text{model}}(W, \alpha)$ using the scheme described above. By varying the final Kp_2^* models we looked for the model that provided the best fit between modeled fluxes and those observed at the injection peak, $J_E^2(W, \alpha)$. We use logarithmic standard deviation between the observed flux and the modeled flux, $\sigma = \sum |\log(J_E^{\text{model}}/J_E^1)|$, summed over energies and pitch angles. Only bins with $E > 5$ keV are used, because the presence of a field-aligned potential drop may cause serious distortions for low-energy and low-pitch-angle particles (see Fig. A1a). The results of the comparison for the best fit are shown in Fig. A1. Calculated standard deviations for the resulting Kp pairs are presented in Table 1. The σ values are in the range 0.20–0.25 when including the contribution from low pitch angles ($< 7.5^\circ$); for larger pitch angles only the standard deviation is much smaller, $\sigma \approx 0.1$. For comparison, the difference between the observed initial and observed accelerated distributions, $\sigma = \sum |\log(J_E^2/J_E^1)|$, is 0.45.

Acknowledgements. The preliminary AE index data were made available at Kyoto WDC-C data base. The electric field data are thanks to Cluster EFW instrument (M. Andre, PI). DMSP data was produced JHU/APL. ACE spacecraft data provided by N. Ness (Bartol Research Institute). The midlatitude magnetometer data was provided by INTERMAGNET. The work by S. V. Apatenkov was supported by INTAS-05-109-4496 grant. The research was also supported by INTAS 03-51-3738 grant and president grant for Leading Scientific Schools 8667.2006.5. S. V. Apatenkov and V. A. Sergeev thank the Austrian Academy of Sciences for the support during their stay in Graz.

Topical Editor I. A. Daglis thanks two referees for their help in evaluating this paper.

References

- Arnoldy, R. L. and Chan, K. W.: Particle substorm observed at the geostationary orbit, *J. Geophys. Res.*, 74, 5019–5028, 1969.
- Baker, D. N., Higbie, P. R., Hones, E. W., and Belian, R. D.: High-resolution energetic particle measurements at $6.6 R_E$. 3. Low-energy electron anisotropies and short-term substorm predictions, *J. Geophys. Res.*, 83(A10), 4863, 1978.
- Balogh, A., Carr, C. M., Acuna, M. H., et al.: The Cluster magnetic field investigations: overview of in-flight performance and initial results, *Ann. Geophys.*, 19, 1207–1217, 2001, <http://www.ann-geophys.net/19/1207/2001/>.
- Belian, R. D., Gisler, G. R., Cayton, T., and Christensen, R.: High-Z energetic particles at geosynchronous orbit during the great solar proton event series of October 1989, *J. Geophys. Res.*, 97(A11), 16 897–16 906, doi:10.1029/92JA01139, 1992.
- Birn, J., Raeder, J., Wang, Y. L., Wolf, R. A., and Hesse, M.: On the propagation of bubbles in the geomagnetic tail, *Ann. Geophys.*, 22, 1773–1786, 2004, <http://www.ann-geophys.net/22/1773/2004/>.
- Delcourt, D. C. and Moore, T. E.: Precipitation of Ions Induced by Magnetotail Collapse, *J. Geophys. Res.*, 97(A5), 6405–6415, doi:10.1029/91JA03142, 1992.
- Gustafson, G., Andre, M., Carozzi, T., et al.: First results of electric field and density observations by Cluster EFW based on initial months of operation, *Ann. Geophys.*, 19, 1219–1240, 2001, <http://www.ann-geophys.net/19/1219/2001/>.
- Johnstone, A. D., Alsop, C., Burge, S., et al.: Peace: a Plasma Electron and Current Experiment, *Space Sci. Rev.*, 79, 351–398, 1997.
- Kubyshkina, M. V., Sergeev, V. A., and Pulkkinen, T. I.: Hybrid Input Algorithm: An event-oriented magnetospheric model, *J. Geophys. Res.*, 104(A11), 24 977–24 994, doi:10.1029/1999JA900222, 1999.
- Kubyshkina, M. V., Sergeev, V. A., Dubyagin, S. V., Wing, S., Newell, P. T., Baumjohann, W., and Lui, A. T. Y.: Constructing the magnetospheric model including pressure measurements, *J. Geophys. Res.*, N6, 1070, doi:10.1029/2001JA900167, 2002.
- Li, X., Baker, D. N., Temerin, M., Reeves, G. D., and Belian, R. D.: Simulation of dispersionless injections and drift echoes of energetic electrons associated with substorms, *Geophys. Res. Lett.*, 25(20), 3763–3766, doi:10.1029/1998GL900001, 1998.
- Li, X., Sarris, T. E., Baker, D. N., and Peterson, W. K.: Simulation of energetic particle injections associated with a substorm on August 27, 2001, *Geophys. Res. Lett.*, 30(N1), 1004, doi:10.1029/2002GL015967, 2003.
- Lyons L. R., Zesta, E., Xu, Y., Sanchez, E. R., Samson, J. C., Reeves, G. D., Ruohoniemi, J. M., and Sigwarth, J. B.: Auroral poleward boundary intensifications and tail bursty flows: A manifestation of a large-scale ULF oscillation?, *J. Geophys. Res.*, 107(A11), 1352, doi:10.1029/2001JA000242, 2002.
- Lyons, L. R., Wang, C.-P., Nagai, T., Mukai, T., Saito, Y., and Samson, J. C.: Substorm inner plasma sheet particle reduction, *J. Geophys. Res.*, 108(A12), 1426, doi:10.1029/2003JA010177, 2003.
- Moore, T. E., Arnoldy, R. L., Feynman, J., and Hardy, D. A.: Propagating substorm injection fronts, *J. Geophys. Res.*, 86, 6713–6726, 1981.
- Nakamura, R., Baumjohann, W., Brittnacher, M., Sergeev, V. A., Kubyshkina, M., Mukai, T., and Liou, K.: Flow bursts and auroral activations: Onset timing and foot point location, *J. Geophys. Res.*, 106(A6), 10 777–10 790, doi:10.1029/2000JA000249, 2001a.
- Nakamura, R., Baumjohann, W., Schödel, R., Brittnacher, M., Sergeev, V. A., Kubyshkina, M., and Mukai, T., and Liou, K.: Earthward flow bursts, auroral streamers, and small expansions, *J. Geophys. Res.*, 106(A6), 10 791–10 802, doi:10.1029/2000JA000306, 2001b.
- Ohtani, S.-I.: Earthward expansion of tail current disruption: Dual-satellite study, *J. Geophys. Res.*, 103, 6815–6825, 1998.
- Reeves, G. D., Belian, R. D., and Fritz, T. A.: Numerical tracing of energetic particle drifts in a model magnetosphere, *J. Geophys. Res.*, 96(A8), 13 997–14 008, doi:10.1029/91JA01161, 1991.
- Reeves, G. D., Henderson, M. G., McLachlan, P. S., Belian, R. D., Friedel, R. H. W., and Korth, A.: Radial propagation of substorm injections, *Proceedings of the 3rd International Conference on Substorms*, Versailles, France, 12–17 May 1996, 579–584, 1996.
- Rème, H., Aoustin, C., Bosqued, J. M., et al.: First multispacecraft ion measurements in and near the Earth's magnetosphere with

- the identical Cluster ion spectrometry (CIS) experiment, *Ann. Geophys.*, 19, 1303–1354, 2001, <http://www.ann-geophys.net/19/1303/2001/>.
- Sarris, T. E., Li, X., Tsaggas, N., and Paschalidis, N.: Modeling energetic particle injections in dynamic pulse fields with varying propagation speeds, *J. Geophys. Res.*, 107(A3), doi:10.1029/2001JA900166, 2002.
- Schödel, R., Nakamura, R., Baumjohann, W., and Mukai, T.: Rapid flux transport and plasma sheet reconfiguration, *J. Geophys. Res.*, 106, 8381–8390, 2001.
- Sergeev, V. A., Vagina, L. I., Elphinstone, R. D., Murphree, J. S., Hearn, D. J., Cogger, L. L., and Johnson, M. L.: Comparison of UV optical signatures with the Substorm Current Wedge predicted by an inversion algorithm, *J. Geophys. Res.*, 101(A2), 2615–2628, doi:10.1029/95JA00537, 1996a.
- Sergeev, V. A., Angelopoulos, V., Gosling, J. T., Cattell, C. A., and Russell, C. T.: Detection of localized, plasma-depleted flux tubes or bubbles in the midtail plasma sheet, *J. Geophys. Res.*, 101(A5), 10 817–10 826, doi:10.1029/96JA00460, 1996.
- Sergeev, V. A., Shukhtina, M. A., Rasinkangas, R., Korth, A., Reeves, G. D., Singer, H. J., Thomsen, M. F., and Vagina, L. I.: Event study of deep energetic particle injections during substorm, *J. Geophys. Res.*, 103(A5), 9217–9234, doi:10.1029/97JA03686, 1998.
- Sergeev, V. A., Liou, K., Meng, C.-I., Newell, P. T., Brittnacher, M., Parks, G., and Reeves, G. D.: Development of auroral streamers in association with localized impulsive injections to the inner magnetotail, *Geophys. Res. Lett.*, 26(3), 417–420, doi:10.1029/1998GL900311, 1999.
- Sergeev, V. A., Sauvaud, J.-A., Popescu, D., Kovrazhkin, R. A., Liou, K., Newell, P. T., Brittnacher, M., Parks, G., Nakamura, R., Mukai, T., and Reeves, G. D.: Multiple-spacecraft observation of a narrow transient plasma jet in the Earth's plasma sheet, *Geophys. Res. Lett.*, 27(6), 851–854, doi:10.1029/1999GL010729, 2000.
- Sergeev, V. A., Yahnin, D. A., Liou, K., Thomsen, M. F., and Reeves, G. D.: Narrow Plasma Streams as a candidate to populate the inner magnetosphere, *Geophys. Monogr. Ser.*, p. 155, 2005.
- Smets, R., Delcourt, D., Sauvaud, J. A., and Koperski, P.: Electron pitch angle distributions following the dipolarization phase of a substorm: Interball-Tail observations and modeling, *J. Geophys. Res.*, 104(A7), 14 571–14 576, doi:10.1029/1998JA900162, 1999.
- Thomsen, M. F., Birn, J., Borovsky, J. E., Morzinski, K., McComas, D. J., and Reeves, G. D.: Two-satellite observations of substorm injections at geosynchronous orbit, *J. Geophys. Res.*, 106(A5), 8405–8416, doi:10.1029/2000JA000080, 2001.
- Tsyganenko, N. A.: A magnetospheric magnetic field with a warped tail current sheet, *Planet. Space Sci.*, 37, 5–20, 1989.
- Tsyganenko, N. A.: Modeling the Earth's magnetospheric magnetic field confined within a realistic magnetopause, *J. Geophys. Res.*, 100, 5599–5612, 1995.
- Tsyganenko, N. A. and Mukai, T.: Tail plasma sheet models derived from Geotail particle data, *J. Geophys. Res.*, 108(A3), 1136, doi:10.1029/2002JA009707, 2003.
- Wilken, B., Daly, P. W., Mall, U., et al.: First results from the RAPID imaging energetic particle spectrometer on board Cluster, *Ann. Geophys.*, 19, 1355–1366, 2001, <http://www.ann-geophys.net/19/1355/2001/>.
- Zaharia, S., Birn, J., Friedel, R. H. W., Reeves, G. D., Thomsen, M. F., and Cheng, C. Z.: Substorm injection modeling with nondipolar, time-dependent background field, *J. Geophys. Res.*, 109, A10211, doi:10.1029/2004JA010464, 2004.